Mapping of gold-related alteration minerals and linear structures using ASTER data in the Giyani Greenstone Belt, South Africa

Nndanduleni Muavhi[1], Mbofholowo Emmanuel Mavhungu[2]

[1]Department of Geology and Mining, University of Limpopo, South Africa, nndandulenimuavhi@gmail.com
[2]GeoAtla, South Africa, mbofho@icloud.com

DOI: http://dx.doi.org/10.4314/sajg.v9i2.17

Abstract

This paper focuses on the mapping of alteration minerals and linear structures associated with gold mineralization in the Giyani Greenstone Belt (GGB). Spectral Information Divergence (SID) and Linear Spectral Unmixing (LSU) classification algorithms were applied to the ASTER data using image extracted endmember spectra which match the spectral profiles of predominant alteration minerals (biotite and calcite) related to gold mineralization in the GGB. Directional convolution filters were also applied to the ASTER data to extract structural lineaments that may be related to gold mineralization. In addition, Fry analysis of known gold occurrences in the GGB was conducted to determine the major distribution patterns along which gold mineralization have occurred. LSU and SID results show several pixels classified as alteration minerals corresponding to known gold occurrences. SID results also show minerals overlapping into the gneissic rock, which is a rare host of gold mineralization in the study area. On the other hand, LSU results show high abundances of calcite and biotite generally confined within the mafic-ultramafic greenstone rocks, which have been hypothesized as the source of gold-mineralized fluids in the GGB. In general, LSU show distinct broad regions classified as alteration minerals corresponding to known gold occurrences that have been previously reported to host these alteration minerals. Directional convolution filters enabled the extraction of predominately NE-SW oriented linear structures, including the major shear zone which is associated with gold mineralization in the GGB. Fry analysis revealed three major distribution patterns: N-S, NE-SW, ENE-WSW along which gold mineralization have occurred. These patterns correspond to major lineaments associated with gold mineralization reported in the previous structural studies of the GGB.

Keywords: *giyani greenstone belt; remote sensing; ASTER; hydrothermal alteration minerals; linear structures; fry analysis*

1. Introduction

Remote sensing has been widely used for structural mapping (Mwaniki et al., 2015; Taoufik et al., 2016; Wambo et al., 2016; Hermi et al., 2017; Hewson et al., 2017) and hydrothermal deposits exploration (Loughlin, 1991; Huntington, 1996; Gabr et al., 2010; Hosseinjani and Tangestani, 2011; Honarmand et al., 2011; Liu et al., 2017; Sheikhrahimi et al., 2019). The spatial position and orientation of lineaments are considered essential guide predictions of hydrothermal fluids-related ore deposits as they represent the connecting channels between ore-forming fluids and ore deposits (Lee and Wiltschko, 2000; Jelsma et al., 2004 and 2009). This is based on the notion that hydrothermal fluids find their pathways through these deeply penetrating weak zones such as faults, shear zones, lithological contacts and dykes. As a result, these structurally weak zones form focal points for hydrothermal fluids-related deposits such as gold and are targeted during exploration (Pour et al., 2016; Sheikhrahimi et al., 2019). In remotely sensed images, linear structures are enhanced spatially through edge detection techniques such as directional filters (Haralick et al., 1987; Aboelsoud, 2014).

The metal-rich hydrothermal fluids result in alteration of the host rock (Harvey and Vitaliano, 1964; Ashley, 1974). The application of remote sensing in exploration of hydrothermal deposits depends on the capacity and capability of a remote sensor to detect spectral signatures related to hydrothermal alteration zones (Gabr et al., 2010; Hosseinjani and Tangestani, 2011; Honarmand et al., 2011; Liu et al., 2017; Sheikhrahimi et al., 2019). The alteration zones envelope the orebody and the intensity of alteration increases with proximity to the mineralization. These zones are associated with alteration minerals such as kaolinite, alunite, chlorite, biotite, pyrophyllite, hematite, muscovite and calcite (Harvey and Vitaliano, 1964; Ashley, 1974). Most of these minerals are characterized by diagnostic spectral features in the visible-near infrared (VNIR) and short-wave infrared (SWIR) spectral regions of the electromagnetic spectrum (Clark et al., 2007; Kokaly et al., 2017). As a result, several authors (Rowan and Mars, 2003; Kaliknowski and Oliver, 2004; Gabr et al., 2010; Honarmand et al., 2011; Liu et al., 2017; Sheikhrahimi et al., 2019) have used VNIR and SWIR bands of different sensors for mapping hydrothermal alteration zones.

Advanced Spaceborne Thermal Emission and Reflection Radiometer (ASTER) is an advanced multispectral remote imaging sensor which was launched on board the Terra satellite in December 1999. ASTER covers a wide spectral region with 14 bands ranging from the visible to thermal infrared region. The spatial resolution varies with spectral region: 15 m in the VNIR, 30 m in the SWIR, and 90 m in the thermal infrared (TIR). These three spectral regions have three, six, and five bands, respectively. Each ASTER scene has a swath width of 60 km^2 (Richards and Jia, 2005). The SWIR bands of ASTER sensor are more contiguous compared to those of Landsat and yield relatively increased accuracy in spectral discrimination of alteration minerals (Crósta and Filho, 2003); which makes ASTER relatively superior for mapping hydrothermal alteration minerals.

Mineral mapping using remote sensing is achieved by comparing the spectral similarities of mineral spectra and image pixel spectra using classification algorithms (Hosseinjani and Tangestani,

2011; Honarmand et al., 2011; Sheikhrahimi et al., 2019). There are two general types of classification algorithms that are used in remote mapping: per-pixel and sub-pixel algorithms (Richards and Jia, 2005). Per-pixel algorithms such as Spectral Information Divergence (SID) assign a pixel to a single ground cover class (Du et al., 2004); while, sub-pixel algorithms such as Linear Spectral Unmixing (LSU) quantify target materials in every pixel of an image by treating a pixel as a mixture of materials (Boardman et al., 1995). Often times, a pixel of low spatial resolution, is rarely composed of one material and appear to be a mixture of the energy reflected from different materials. As a result, a sub-pixel classification has recently attracted increasing interest in alteration mapping (Gabr et al., 2010; Hosseinjani and Tangestani, 2011; Honarmand et al., 2011; Tayebi and Tangestani, 2014).

To the authors' knowledge, the GGB has no published previous remote sensing studies concerning hydrothermal alteration mapping. This may be due to paucity of lithological outcrops. Consequently, the main aim of this study was to examine the ability of per-pixel (SID) and sub-pixel (LSU) classification algorithms in the mapping of hydrothermal alteration minerals in the GGB using ASTER data. The secondary aims were (1) to implement directional convolution filters to ASTER data to map linear structures and (2) to conduct Fry analysis of known gold occurrences to determine the major distribution patterns along which gold mineralization have occurred in the GGB.

2. Study area and geological setting

The GGB is situated in the north eastern edge of the Archean Kaapvaal Craton immediately adjacent to the Hout River Shear Zone and proximal South Marginal Zone of Limpopo Mobile Belt (Kramers et al., 2014) (Fig. 1). The GGB is approximately 15 km wide and 70 km long. The belt is dominated by supra-crustal rocks of the Giyani Group, which is mainly characterized by mafic and ultramafic rocks with minor intercalations of metasedimentary rocks and felsic volcanics (Kröner et al., 2000). The metasedimentary rocks include quartzite, banded iron formation (BIF) and rare dolomite. The Giyani Group is bordered to the west and east by migmatized gneisses and to the south by younger granitoids (McCourt and Van Reenen, 1992) (Fig. 1).

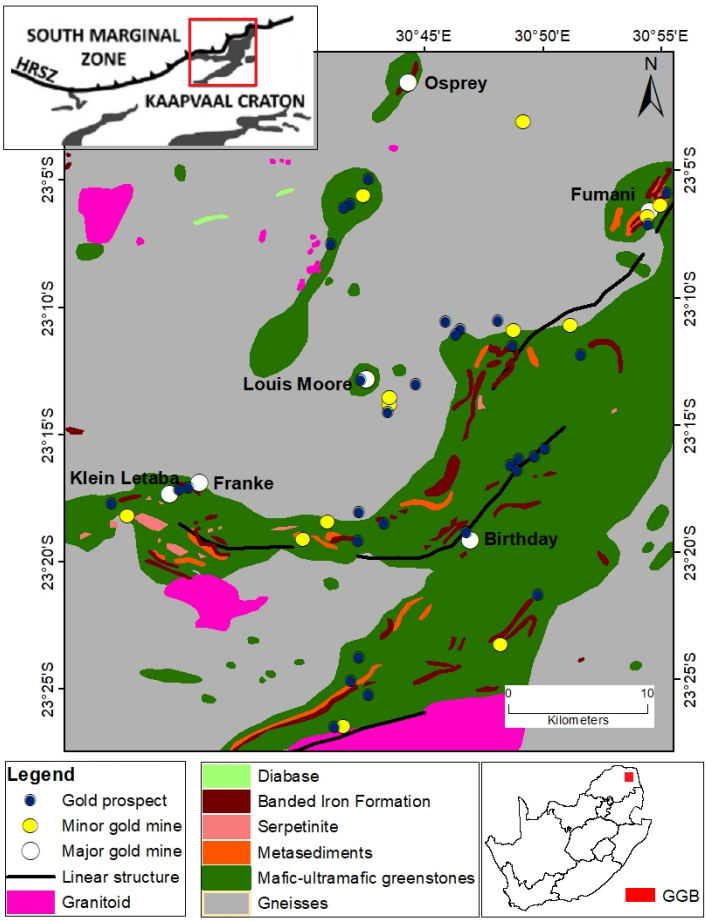

Figure 1: Simplified geological map of the Giyani Greenstone Belt (after Vorster, 1979). Linear structures are fault/shear zones, adopted from McCourt and Van Reenen (1992). Gold occurrences were adopted from Carranza et al. (2015).

Detailed structural studies of McCourt and Van Reenen (1992) and De Wit et al. (1992) revealed that the GGB is characterized by ductile shear zones parallel to regional foliation that form the main regional structural grain of the GGB. This regional structure is characterized by an upright to steeply oblique mineral elongation lineation that plunges northwards. The regional foliation forming the main structural grain of the GGB is axial planar to isoclinal and sheath folds, at the regional and local scale, oriented NE-SW or ESE-WNW with a moderate to steep northerly dip (McCourt and Van Reenen, 1992). The younger ductile deformation phase is characterized by discrete NE-SW and ENE-WSW trending and subvertical dextral strike-slip shearing. This phase is best developed along the southern and northern margins of the belt (McCourt and Van Reenen, 1992). In total, McCourt and Van Reenen (1992) described three ductile deformations: the older penetrative (D1), the younger non-penetrative (D2) and the latest deformation (D3). The D1 resulted in N-trending regional foliation and was responsible for the E-W and ENE-WSW striking shear zones including well-developed mineral lineation. The D2 was superimposed on the D1 structures and can be identified by eastward plunging folds of the regional foliation or related horizontal crinkle lineation. The D3 is associated with NE-SW trending discrete strike-slip shear zones in the southern and northern margins of the belt postdating the granitoid intrusion. The ultramafic-mafic greenstones were affected by all ductile

deformation phases, gneisses by D2 and D3 and granitoid by D3. Gold mineralization is related to D1 and D2 shear zones (McCourt and Van Reenen, 1992; Van Reenen et al., 1997).

3. Gold mineralization

There are more than forty-five known gold occurrences and prospects in the GGB (Carranza et al., 2015). Six of them are inactive gold mines which include Fumani, Franke, Louis Moore, Klein Letaba, Osprey and Birthday. Gold mineralization is hosted along shear zones and close to the contacts of lithologies (Pretorius et al., 1988; McCourt and Van Reenen,1992; De Wit et al., 1992). Gold mineralization along these linear structures occurs in banded iron formations (BIF), quartz veins, quartz-sulphide replacement veins and carbonate veins (Gains et al., 1986). Because wall-rocks of deposits are commonly enriched in K_2O, CO_2 and S, and mineralizing fluids infiltrated wall-rock at lower to upper amphibolite facies pressure-temperature conditions, wall-rocks of auriferous veins in most deposits typically exhibit pervasive biotite and calcite alteration (Gan and Van Reenen, 1995 and 1997; Van Reenen et al., 2014).

The dominant lithologies hosting gold mineralization/auriferous veins are BIF and metasediments xenoliths in mafic-ultramafic greenstones, and greenstones themselves (Carranza et al., 2015). In rare occasions gold deposits are hosted in granitoid gneissic rocks (Fig. 1). The paucity of detailed studies on the genesis of gold mineralization in the GGB impedes proper representation of the source of fluids associated with the deposits. Pretorius et al. (1988) reported that the mineralizing solutions were possibly derived from greenstones themselves; like gold mineralization in other greenstones (Pitcairn et al., 2006). As it can be observed in Figure 1, most gold deposits and prospects are located within mafic-ultramafic greenstones which supports the likelihood of greenstones being the source.

4. Materials and methods

4.1. ASTER data

The datasets used in this study are ASTER Level 1B cloud-free scenes with Granule IDs of AST_L1B_00310042004081157 and AST_L1B_00304092003081333. The two scenes were acquired on 04 October 2003 and 09 April 2003, respectively. These ASTER data products were retrieved on (https://lpdaac.usgs.gov) maintained by the NASA Land Processes Distributed Active Archive Center (LPDAAC) at the USGS/Earth Resources Observation and Science (EROS) Center, Sioux Falls, South Dakota. Level 1B products contain radiometrically calibrated and geometrically co-registered data for all ASTER channels. Table 1 shows the spectral resolution of the nine ASTER bands used in this study. The pre-processing and classification of ASTER images, detailed in the following sections, were carried out using Environment for Visualizing Image (ENVI) 5.0 software.

Table 1: Wavelengths and spatial resolution of ASTER bands (Richards and Jia, 2005).

Spectral region	Band number	Wavelength range (μm)	Spatial resolution (m)
VNIR	1	0.52-0.60	15
	2	0.63-0.69	
	3N	0.78-0.86	
	3B	0.78-0.86	
SWIR	4	1.60-1.70	30
	5	2.145-2.185	
	6	2.185-2.225	
	7	2.235-2.285	
	8	2.295-2.365	
	9	2.360-2.430	

4.1.1. Image pre-processing

The VNIR and SWIR bands of individual scenes were stacked together to build two multiband images. In the process of band stacking, the SWIR bands were resampled with the VNIR bands to be of 15 m spatial resolution using the nearest neighbor resampling technique. In general, during band stacking, bands having different spatial resolutions are resampled to be of the same spatial resolution. Ideally, bands with low spatial resolution are resampled with bands having high spatial resolution to enhance the general spatial resolution which is crucial for subsequent mapping (Research Systems Inc, 2008; Muavhi, 2020).

The two multiband images were mosaicked to form a single multiband image. The resultant multiband image was then subset to cover the study area. The log residuals calibration was therefore applied to the subset image to convert Top of Atmosphere (TOA) to Bottom of Atmosphere (BOA) reflectance (Green and Craig, 1985). Conversion from TOA to BOA reflectance is essential for multiband image processing when you want to detect the presence of mineral targets using mineral reference spectral library or when you want to compare image extracted endmembers with mineral reference spectral library as spectral libraries are nearly always in BOA reflectance (Clark et al., 2007; Kokaly et al., 2017).

4.1.2. Endmember extraction

Following the methodologies of Boardman and Kruse (1994) and Boardman et al. (1995), the stepwise procedure for image endmember extraction involved minimum noise fraction (MNF), pixel purity index (PPI), n-Dimensional visualizer and spectral analyst. The MNF was implemented to the input dataset containing log residuals-calibrated multiband image. The resultant nine MNF components had eigenvalues of greater than one, and thus all the bands were retained for subsequent data processing. PPI was then applied to the MNF images with 10000 default projection of the scatter plot and a default threshold factor of 2.50 (Research Systems Inc, 2008). After calculation of PPI, the image derived pure pixels were exported as regions of interest (ROIs) to be used for n-Dimensional visualization and endmember extraction. The coordination of the points in n-D space consists of ‘n’ values that are simply the spectral reflectance values in each band for a given pixel (Research Systems

Inc, 2008). The distributions of these points in n-D space were used to estimate the number of endmembers in the image. A total of 13 endmembers extracted from n-D visualizer. To identify the extracted endmembers that correspond to the alteration minerals of interest, the ASTER resampled mineral reference spectra from USGS spectral library (Clark et al., 2007) were used for comparative analysis with the aid of spectral analyst technique. The output of the spectral analyst is a list of the reference spectra ranked in order of best-to-worst match with the selected endmember. The score ranges from 0 to 1 for each input reference spectrum, with 1 equaling a perfect match with the extracted endmember (Research Systems Inc, 2008). From the 13 image extracted endmembers, one endmember with diagnostic absorption feature in band 8, attained the highest fitting score with calcite (0.889). Another endmember with absorption features in bands 3 and 8 attained the highest fitting score with biotite (1.000) (Fig. 2). Calcite and biotite are associated with most gold deposits in the GGB (Van Reenen et al., 2014;).

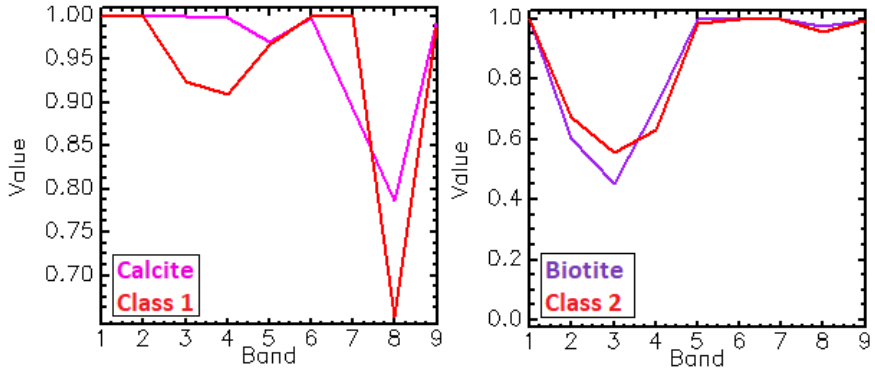

Figure 2: Known mineral spectra vs image extracted endmembers (red).

4.1.3. Spectral Information Divergence

SID is a per-pixel algorithm that assigns a pixel to a single ground cover class. SID measures spectral variability of a single mixed pixel from a probabilistic point of view (Du et al., 2004). This algorithm uses a divergence measure to match image pixels to endmember spectra. The smaller the divergence measure threshold, the more likely the pixels and endmember match (Du et al., 2004). Pixels with a measurement greater than the specified maximum divergence threshold are not classified (Research Systems Inc, 2008). SID results in a classified image showing the best fit between pixels and endmembers. In addition, rule images are provided showing the divergence measure values between each pixel and each endmember. The black pixels in the rule image present smaller divergence values, and therefore more similar to the spectra of endmembers (Research Systems Inc, 2008). The advantage of mapping using rule images is that the user can generate several classification images from various divergence measure thresholds, without having to recalculate the entire classification, by applying density slice thresholds to the rule images (Research Systems Inc, 2008).

To date, there is no general agreement as to how to ascertain a definitive threshold value for comparing pixel and endmember spectra in SID classification. In general, the selection of threshold values is quite subjective and user-defined (Tangestani et al., 2008; Honarmand et al., 2013). In ENVI

software, the default maximum divergence threshold of 0.05 (Research Systems Inc, 2008) can be considered as the highest acceptable threshold between endmember and pixel spectra in the SID classification. In this study, a divergence threshold of 0.015 was selected and used for hydrothermal alteration mapping. This value represents a relatively lower threshold value to the default divergence threshold (0.05). The smaller the divergence threshold value, the lower the number of classified pixels and the more likely the classified pixels represent minerals in question in the ground (Du et al., 2004). In this regard, the pixels with divergence values of ≤0.015 are more similar to the alteration mineral spectra. Density slice thresholds in the range of 0.000-0.010 and 0.010-0.015 were performed on the classified rule images of biotite and calcite for best viewing and interpretation.

4.1.4. Linear Spectral Unmixing

LSU is a sub-pixel algorithm that quantifies target materials in every pixel of an image by treating a pixel as mixture of materials (Boardman et al., 1995). LSU achieves unmixing by assuming that the reflectance at each pixel of the image is the linear proportioned-weighted combination of the reflectance of each material present within a pixel. In other words, given the input image and the endmembers, LSU solves for the abundance values of each endmember for every pixel in the input image. The number of endmembers can vary considerably depending on the number of bands and spectral complexity of image. However, the number of endmembers cannot exceed the number of bands (Research Systems Inc, 2008).

The LSU results in series of grey-scale images, one for each mapped material depending on the selected endmembers, plus a root-mean-square error (RMSE) image. The higher abundances of endmembers are represented as brighter pixels. Also, higher errors for RMSE image appear as brighter pixels (Research Systems Inc, 2008). When image extracted endmembers exceed the number of bands in the input dataset, endmembers can be used interchangeably to conduct LSU classification and the resultant RMSE image can be investigated for classification errors for every attempt. The combination of endmembers that provides lowest maximum error can therefore be used for final LSU classification and subsequent interpretation. In addition, well characterized LSU results have many pixels with values ranging from 0.0 to 1.0; where a pixel having 1.0 value for particular endmember indicates that the pixel contains 100 % of that particular material (Research Systems Inc, 2008).

As previously stated, a total of 13 endmembers were extracted from image derived pure pixels. Since the number of endmembers (13) exceeded the number of bands (9) in the multiband image, two mineral endmember classes (calcite and biotite) were given first priority, while the remaining eleven were given second priority. Seven of the eleven endmembers assigned second priority were combined interchangeably with calcite and biotite to have nine endmembers (equaling the number of bands in the multiband image) for every LSU classification trial. The resultant RMSE image was investigated, for every trial, to determine classification error until the lowest maximum error value of 0.01 was achieved.

4.2. Mapping of linear structures

4.2.1. Convolution filtering

In remote sensing, linear structures are enhanced spatially through edge detection techniques such as convolution filters (Haralick et al., 1987; Jensen, 2005; Research Systems Inc, 2008; Aboelsoud, 2014). These filters delineate the edges and make the shapes and details comprising the image more noticeable and easier to analyze (Jensen, 2005). The directional nature of geological structures emphasizes the need for directional filtering to obtain maximum structural mapping efficiency (Tripathi and Gokhale, 2000). Consequently, the directional convolution filtering was used for mapping linear structures in the study area.

Following the methodology of Abdullah et al. (2013), visual inspection of the individual bands in the multiband image was carried out, and based on the ability to identify linear features, band 7 was selected. The second step of the methodology was to select the kernel matrix type. For this purpose, different types of kernel matrices (3 x 3, 5 x 5 and 7 x 7) were tested. Based on visual comparison, the 5 x 5 kernel matrix provided better results in terms of edge enhancement and linear emphasis. Consequently, four major directional filters: N-S (0°), NE-SW (45°), E-W (90°) and NW-SE (135°) with 5 x 5 kernel matrix were applied to band 7 of ASTER. The four major directional filters were used because they allow for detection of lineaments in all possible directions (Hermi et al., 2017).

4.2.2. Fry analysis

Fry analysis is used to assess spatial distribution patterns of mineral occurrences and potential controlling structures at regional and local scale (Fry, 1979). The spatial distribution is analyzed, maintaining a consistent north, by placing every mineral occurrence at an origin and plotting all other occurrences relative to this origin. This method results in an unbiased geometrical examination of the distance and direction between each mineralized occurrence, and construction of rose diagram showing preferred directions of spatial continuity that may correspond to potential controlling structures responsible for mineralization (Vearncombe and Vearncombe, 2002).

The aims of Fry analysis were to evaluate if the major distribution patterns revealed by this method correspond (1) to the trends of mapped linear structures using directional convolution filtering and (2) to the mineralization controlling structures reported in previous structural studies (McCourt and Van Reenen, 1992; De Wit et al., 1992). The locations of forty-nine gold occurrence sites were compiled from the database of the South African Council for Geoscience. These occurrences can be classified into gold mines and prospects. Prior to implementation of Fry spatial analysis, the data were separated into gold mines (19) and prospects class (30), including composite class comprising both mines and prospect (49). The points of each class were horizontally translated following the methodology described by Vearncombe and Vearncombe (1999). The resulted translation points of the three classes were then used to construct rose diagrams depicting the potential spatial distribution patterns of gold mineralization.

5. Results and Discussions

5.1. Alteration mineral mapping

To map the alteration minerals, SID and LSU classification algorithms were applied on the log residuals-calibrated VNIR-SWIR multiband image of ASTER. These classifications were applied based on the comparison of image pixel spectrum with the spectra of known endmembers extracted from image. The extracted endmembers correspond to the spectral profiles of biotite and calcite. These minerals are associated with hydrothermal alteration of gold mineralization in the GGB (Van Reenen et al., 2014; Gan and Van Reenen, 1997 and 1995), and therefore can be used for hydrothermal alteration mapping. As stated under the methodology, only pixels with divergence measure values of ≤0.015 with alteration mineral spectra were classified and discussed hereafter.

The pixels achieved lowest divergence measure value (DMV) of 0.003 and 0.005 with biotite and calcite spectrum respectively, which suggest closer matches between the classified pixels and alteration minerals. For biotite, pixels with divergence measure values in the range of 0.003-0.010 and 0.010-0.015 are in blue and magenta, respectively (Fig. 3a). A distinct broad clustering of biotite can be observed in an area situated NE of Birthday Mine corresponding to several gold prospects. Also, a few discrete clustering regions exist in the NW of the area (Fig. 3a). However, these regions spatially fall within the gneissic rock, a rare host of gold occurrences in the GGB. On the other hand, pixels classified as calcite in the DMV range of 0.005-0.010 and 0.010-0.015 are in cyan and magenta, respectively (Fig. 3b). Few pixels classified as calcite correspond to areas of gold occurrences. However, calcite has no distinct broad regions of clustering and appear as scattered pixels throughout the study area.

The results of LSU classification for each endmember were indicated by the fraction of that endmember in each pixel. The gray scale image of biotite (Fig. 3c) revealed that the values of pixels were up to 53%. Pixels which contain biotite in the range of 50-53% are shown in red and pixels with 45-50% in magenta. Pixels showing high abundances of biotite (50-53%) correspond to gold mines such as Fumani, Birthday and Osprey, including several gold prospects of previous study (Carranza et al., 2015). In addition, the distinct broad biotite clustering situated in the NE of Birthday Mine corresponding to several gold prospects in Figure 3a can also be observed in the LSU biotite map (Fig. 3c). Generally, the LSU biotite map is almost similar to the SID biotite map. However, the distribution of biotite in the LSU map is well confined in the boundary of the greenstones, and do not overlap into granitoids and gneissic rocks in the southern margins of the study area. The gray scale image of calcite (Fig. 3d) revealed that the values of pixels were up to 48%. Pixels in the range of 44-48% and 40-44% are in blue and pink, respectively. Like biotite, pixels showing high abundances of calcite correspond to gold mines (Fumani, Birthday and Osprey) and prospects in the LSU map (Fig. 3d). Contrary to the SID map in which calcite is scattered throughout the study area (Fig. 3a), LSU map shows distinct clustering regions of calcite. Furthermore, the pixels showing high abundances of calcite in the southern parts of the study area are well confined within the greenstones (Fig. 3d).

The greenstones have been hypothesized as the source of gold mineralizing solutions in the GGB (Pretorius et al., 1988).

Based on the estimated relative abundances, the alteration minerals appear together in most pixels. This spatial distribution relationship of biotite and calcite confirms the pervasive biotite and calcite alteration observed in most gold deposits of the GGB (Van Reenen et al., 2014; Gan and Van Reenen, 1997 and 1995; Pretorius et al., 1988).

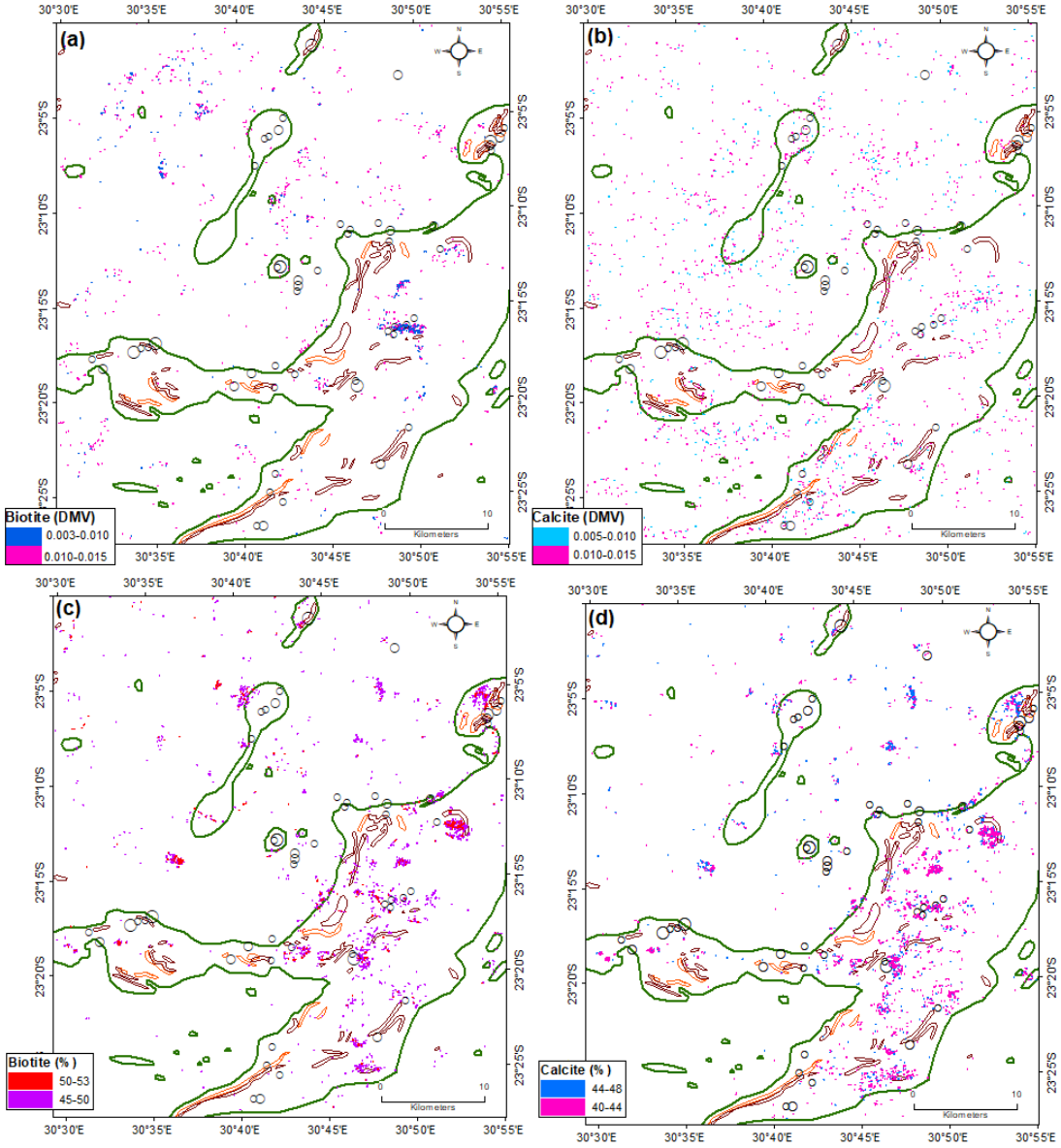

Figure 3: Distribution map of alteration minerals derived from SID (a and b) and LSU (c and d). The greenstones (green), BIF (dark umber), metasediments (fire red) and gold occurrences (black circles) are superimposed on the map.

5.2. Linear structure mapping

The spatial position and orientation of linear structures are considered essential guide predictions of hydrothermal fluids-related ore deposits as they represent the connecting channels between ore-forming fluids and ore deposits (Lee and Wiltschko, 2000). Therefore, mapping lineaments in the

GGB can provide essential information for exploration of gold mineralization and identification of new prospects. The four major directional filters that were applied on band 7 of ASTER using 5 x 5 kernel matrix revealed several lineaments in the study area. The most pronounced linear structures in images derived from directional filters were extracted and displayed in Figure 4.

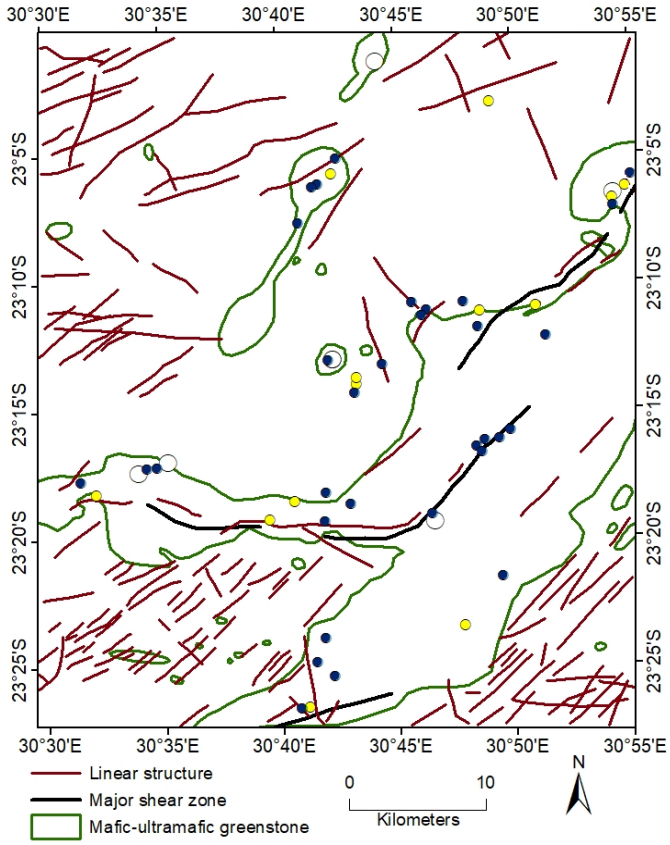

Figure 4: Linear structures extracted from study area using directional filters. Major gold mines (white circles), minor gold mines (yellow circles) and gold prospects (blue circles) are superimposed on the map.

The dominant trend of linear structures in the area is NE-SW. This orientation is best developed in the southern and north western margins of the GGB (Fig. 4). Most of these linear structures in these parts of the study area occur in the granitoid and gneissic rocks shown in Figure 1. These rocks are rare host of gold mineralization in the GGB (Fig. 1). According to McCourt and Van Reenen (1992), the linear structures in the southern and northern margins are related to younger ductile deformation phase (D_3) which is not related to controlling mineralization lineaments. In addition, the directional filters managed to detect and allow the extraction of lineament corresponding to major shear zone associated with gold mineralization in the belt (Fig. 4).

Fry analysis of known gold occurrences in the GGB was conducted to determine the major distribution patterns along which gold mineralization have occurred. As stated under the methodology, the gold occurrence data were classified into three classes (gold mines, gold prospects and composite class). The construction of rose diagrams from translation points of the three classes helped to interpret the spatial patterns of gold mineralization (Fig. 5). The results of Fry analysis show

that the three classes correspond in terms of the major distribution trends which are oriented N-S (0°/7°), NE-SW (35°) and ENE-WSW (65°) (Fig. 5). These distribution patterns are consistent with the major lineaments responsible for providing passage for auriferous rich hydrothermal fluids in the GGB (McCourt and Van Reenen,1992; De Wit et al., 1992). The NE-SW orientation is also observed in the younger linear structures (D_3) in the southern edge and northern contact of the study area. Most of these linear structures occur in the gneissic rock (Fig. 1) and have no known relationship with gold mineralization (McCourt and Van Reenen, 1992). In this regard, linear structures having trends revealed as favorable for gold mineralization by the Fry analysis and occurring in or proximal to mafic-ultramafic greenstones can be targeted for future exploration work.

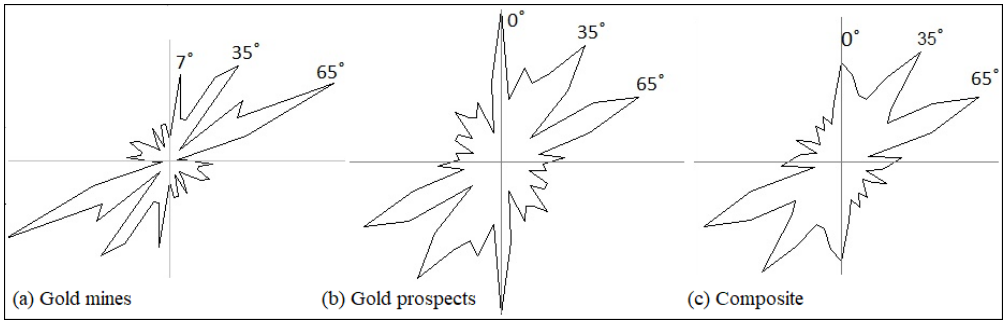

Figure 5: Rose diagrams showing major distribution patterns of the three classes.

6. Conclusions

The aims of this study were to map alteration minerals and linear structures associated with gold mineralization in the GGB using ASTER data. Alteration minerals were mapped using per-pixel (SID) and sub-pixel (LSU) classification algorithms. Linear structures were extracted from ASTER data using directional convolution filters. In addition, Fry analysis of known gold occurrences was conducted to determine major distribution patterns along which gold mineralization have occurred in the GGB.

SID and LSU algorithms classified several pixels corresponding to known gold occurrences as alteration minerals. SID also show alteration minerals overlapping into the gneissic rock, a rare host of gold mineralization in the area. On the other hand, LSU show high abundances of alteration minerals generally confined within the mafic-ultramafic greenstone rocks, which have been hypothesized as the source of gold-mineralized fluids. In general, LSU show distinct broad regions classified as alteration minerals corresponding to known gold occurrences that have been previously reported to host calcite and biotite. Although it cannot be conclusively said that one of these two algorithms performed better than other, this spatial correspondence may indicate the effectiveness of sub-pixel classification in successfully quantifying mineralogical contents of heterogeneous image pixel. A pixel of low to medium spatial resolution rarely represents a single mineral but rather a mixture of minerals in the ground.

Directional convolution filters enabled the extraction of predominately NE-SW oriented linear structures. The NE-SW trend is one of the three major distribution patterns (N-S, NE-SW and ENE-WSW) revealed by Fry analysis as the major orientations along which gold mineralization in the GGB occurred. These patterns correspond to major lineaments associated with gold mineralization from previous studies. In summary, this study has successfully mapped alteration minerals and linear structures in the GGB and show the significance of remote sensing in mapping alteration minerals and linear structures.

7. Acknowledgements

The authors wish to thank the reviewers whose comments and suggestions greatly assisted to improve this research paper.

8. References

Aboelsoud, H.M., 2014, Edge detection using directional filtering: International Journal of Engineering Research and Applications, 4(4), 112-115.

Ashley, R., 1974, Goldfield mining district: Nevada Bureau of Mines and Geology Report, 49-66.

Boardman, J. W., and Kruse, F. A., 1994, Automated spectral analysis: A geological example using AVIRIS data, north Grapevine Mountains, Nevada: Proceedings, ERIM Tenth Thematic Conference on Geologic Remote Sensing, 1407-1418.

Boardman, J.W., Kruse, F.A., and Green, R.O., 1995, Mapping target signatures via partial unmixing of AVIRIS data: Summaries, Fifth JPL Airborne Earth Science Workshop, 23-26.

Clark, R.N., Swayze, G.A., Wise, R., Livo, E., Hoefen, T., Kokaly, R., and Sutley, S.J., 2007, USGS digital spectral library splib06a: U.S. Geological Survey, Digital Data Series.

Carranza, E.J.M., Sadeghi, M., and Billay, A., 2015, Predictive mapping of prospectivity for orogenic gold, Giyani Greenstone Belt (South Africa): Ore Geology Reviews, 71, 703-718.

Crósta, A.P., and Filho, C.R.d.S., 2003, Searching for gold with ASTER: Earth Observation Magazine, 12(5), 38-41.

De Wit, M.J., Van Reenen, D., and Roering, C., 1992, Geologic observations across a tectono-metamorphic boundary in the Babangu Area, Giyani (Sutherland) Greenstone Belt, South Africa. Precambrian Research, 55, 111-122.

Du, H., C.-I. Chang, H. Ren, F.M., D'Amico, J. O., and Jensen, J., 2004, New Hyperspectral Discrimination Measure for Spectral Characterization: Optical Engineering, 43(8), 1777-1786.

Fry, N., 1979, Random point distributions and strain measurement in rocks: Tectonophysics, 60, 89-105.

Gabr, S., Ghulam, A., and Kusky, T., 2010, Detecting areas of high-potential gold mineralization using ASTER data: Ore Geology Reviews, 38, 59-69.

Gains, S.B., McCourt, S., Barton, J.M., Van Reenen, D.D., Pretorius, A.I., and Ehlers, D.L., 1986, The regional geologic setting of the Sutherland Belt, with particular reference to gold mineralization. Unpublished Report No. STK-2587, Council for Geoscience, Pretoria.

Gan, S., and Van Reenen, D.D., 1995, Geology of gold deposits in the Southern Marginal Zone of the Limpopo Belt and the adjacent Sutherland Greenstone Belt, South Africa; Franke Mine. South African Journal of Geology, 98, 263-275.

Gan, S., and Van Reenen, D.D., 1997, Geology of gold deposits in the Southern Marginal Zone of the Limpopo Belt and the adjacent Sutherland Greenstone Belt, South Africa; Klein Letaba. South African Journal of Geology, 100, 73-83.

Green, A.A., and Craig, M.D., 1985, Analysis of aircraft spectrometer data, with logarithmic residuals: Proceedings of the Airborne Imaging Spectrometer Data Analysis Workshop, 111-119.

Haralick, R.M., Sternberg, S.R., and Zhuang, X., 1987, Image analysis using mathematical morphology: IEEE Transactions of Pattern Analysis and Machine Intelligence, 9, 532-550.

Harvey, R., and Vitaliano, C., 1964, Wall-rock alteration in the goldfield district, Nevada: Journal of Geology, 72, 564-579.

Hermi, S.O., Elsheikh, R.F.A., Aziz, M., and Bouaziz, S., 2017, Structural interpretation of lineaments uses satellite images processing-A case study in North-Eastern Tunisia: Journal of Geographic Information System, 9, 440-455.

Hewson, R., Robson, D., Carlton, A., and Gilmore, P., 2017, Geological application of ASTER remote sensing within sparsely outcropping terrain, Central New South Wales, Australia: Cogent Geoscience, 3, 1-22.

Honarmand, M., Ranjbar, H., and Shahabpour, J., 2011, Application of spectral analysis in mapping hydrothermal alteration of the Northwestern Part of the Kerman Cenozoic Magmatic Arc, Iran: Journal of Sciences, Islamic Republic of Iran, 22(3), 221-238.

Honarmand, M., Ranjbar, H., and Shahabpour, J., 2013, Combined use of ASTER and ALI data for hydrothermal alteration mapping in the northwestern part of the Kerman Magmatic Arc, Iran: International Journal of Remote Sensing, 34, 2023-2046.

Hosseinjani, M., and Tangestani, M.H., 2011, Mapping alteration minerals using sub-pixel unmixing of ASTER data in the Sarduiyeh area, SE Kerman, Iran: International Journal of Digital Earth, 4(6), 487-504.

Huntington, J.F., 1996, The role of remote sensing in finding hydrothermal mineral deposits on Earth: In Bock, G.R., and Goode, J.A (Eds.), Evolution of Hydrothermal Ecosystems on Earth (and Mars?). Ciba Foundation Symposium 202. John Wiley & Sons, Chichester, UK.

Jensen, J.R., 2005, Introductory Digital Image Processing-A Remote Sensing Perspective (3rd edition): Pearson Prentice Hall.

Jelsma, H.A., de Wit, M.J., Thiart, C., Dirks, P.H.G.M., Viola, G., Basson, I.J., and Anckar., 2004, Preferential distribution along transcontinental corridors of kimberlites and related rocks of southern Africa: South African Journal of Geology, 107(1-2), 301-324.

Jelsma, H.A., Barnett, W., Richards, S., and Lister, G., 2009, Tectonic setting of kimberlites: Lithos, 112, 155-165.

Kanlinowski, A., and Oliver, S., 2004, ASTER mineral index processing: Remote Sensing Application Geoscience Australia. Australian Government Geoscience Website, http://www.ga.gov.au/image_cache/GA7833.pdf

Kokaly, R.F., Clark, R.N., Swayze, G.A., Livo, K.E., Hoefen, T.M., Pearson, N.C., Wise, R., Benzel, W.M., Lowers, H.A., Driscoll, R.L., and Klein, A.J., 2017, USGS Spectral Library Version 7: U.S. Geological Survey, Data Series.

Kramers, J.D., Henzen, M., and Steide, L., 2014, Greenstone belts at the northernmost edge of the Kaapvaal Craton-Timing of tectonic events and a possible crustal fluid source: Precambrian Research, http://dx.doi.org/10.1016/j.precamres.2014.06.008

Kröner, A., Jaeckel, P., Brandl, G., 2000, Single zircon ages for felsic to intermediate rocks from the Pietersburg and Giyani greenstone belts and bordering granitoid orthogneisses, northern Kaapvaal Craton, South Africa. Journal of African Earth Sciences, 30, 773-793.

Kruse, F.A., Lefkoff, A.B., Boardman, J.B., Heidebrecht, K.B., Shapiro, A.T., Barloon, P.J., and Goetz, A.F.H., 1993, The Spectral Image Processing System (SIPS)-Interactive visualization and analysis of imaging spectrometer data: Remote Sensing of the Environment, 44, 145-163.

Lee, Y.J., and Wiltschko, D.V., 2000, Fault-controlled sequential vein dilation-Competition between slip and precipitation rates in the Austin Chalk, Texas: Journal of Structural Geology, 22, 1247-1260.

Liu, L., Zhou, J., Han, L., and Xu, X., 2017, Mineral mapping and ore prospecting using Landsat TM and Hyperion data, Wushitala, Xinjiang, northwestern China: Ore Geology Reviews, 81(1), 280-295.

Loughlin, W.P., 1991, Principal component analysis for alteration mapping: Photogrammetric Engineering & Remote Sensing, 57(9), 1163-1169.

McCourt, S., and Van Reenen, D.D., 1992, Structural geology and tectonic setting of the Sutherland Greenstone Belt, Kaapvaal Craton, South Africa: Precambrian Research, 55, 93-110.

Muavhi, N., 2020, Evaluation of effectiveness of supervised classification algorithms in land cover classification using ASTER images-A case study from the Mankweng (Turfloop) Area and its environs, Limpopo Province, South Africa: South African Journal of Geomatics, 9(1), 61-74. DOI: http://dx.doi.org/10.4314/sajg.v9i1

Mwaniki, M.W., Matthias, M.S.M, and Schellman, G., 2015, Application of remote sensing technologies to map the structural geology of central region of Kenya: IEEE Journal of Selected Topics in Applied Earth Observations and Remote Sensing, 1-13.

Pitcairn, I.K., Teagle, D.A.H., Craw, D., Olivo, G.R., Kerrich, R., and Brewer, T.S., 2006, Sources of metals and fluids in orogenic gold deposits-Insights from the Otago and Alpine Schists, New Zealand: Economic Geology, 101, 1525-1546.

Pour, B.A., Hashim, M., Makoundi, C., and Zaw, K., 2016, Structural mapping of the Bentong, Raub suture zone using PALSAR remote sensing data, peninsular Malaysia-Implications for sediment-hosted/orogenic gold mineral systems exploration: Resource Geology, 66(4), 368-385.

Pretorius, A.I., Van Reenen, D.D., and Barton, J.M., 1988, BIF-hosted gold mineralization at the Fumani Mine, Sutherland Greenstone Belt, South Africa: South African Journal of Geology, 91, 429-438.

Research Systems Inc, 2008, ENVI Tutorials: Research Systems Inc, Boulder CO.

Richards, J.A., and Jia, X., 2005, Remote Sensing Digital Image Analysis (4th edition): Berlin, Springer-Verlag.

Rowan, L.C., and Mars J.C., 2003, Lithologic mapping in the Mountain Pass, California area using Advanced Spaceborne Thermal Emission and Reflection Radiometer (ASTER) data: Remote Sensing of Environment, 84, 350-366.

Sheikhrahimi, A., Pour, A.B., Pradhan, B., and Zoheir, A., 2019, Mapping hydrothermal alteration zones and lineaments associated with orogenic gold mineralization using ASTER data-A case study from the Sanandaj, Sirjan Zone, Iran: Advances in Space Research, 63(10), 3315-3332.

Tangestani, M.H., Mazhari, N., Agar, B., and Moore, F., 2008, Evaluating Advanced Spaceborne Thermal Emission and Reflection Radiometer (ASTER) data for alteration zone enhancement in a semi-arid area, Northern Shahr-e-Babak, SE Iran. International Journal of Remote Sensing, 29, 2833-2850.

Taoufik, M., Baghdad, B., El Hadi, H., and Langhlimi, M., 2016, Structural interpretation of lineaments by remote sensing and GIS using Landsat 8 data-A case study of Akreuch Area (Morocco), 138(3), 216-224.

Tayebi, M.H., and Tangestani, M.H., 2014, Sub pixel mapping of alteration minerals using SOM neural network model and hyperion data: Earth Science Informatics, 8, 279-291.

Tripathi, N.K., and Gokhale, V.G.K., 2000, Directional morphological image transforms for lineament extraction from remotely sensed images: International Journal of Remote Sensing, 21(17), 3281-3292.

Van Reenen, D.D., Huizenga, J.M., Smit, C.A., and Roering, C., 2014, Fluid–rock interaction during high-grade metamorphism-Instructive examples from the Southern Marginal Zone of the Limpopo Complex, South Africa: Precambrian Research, http://dx.doi.org/10. 1016/j.precamres.2014.06.018.

Vearncombe, S., and Vearncombe, J.R., 2002, Tectonic controls on kimberlite location, South Africa: Journal of Structural Geology, 24, 1619-1625.

Vorster, C.J., 1979, Die geologie van die Klein-Letabagebied Noord-oos Transvaal met spesiale verwysing na die granitiese gesteentes. Unpublished M.Sc. thesis, Rand Afrikaans University, Johannesburg, South Africa.

Wambo, J.D.T., Ganno, S., Ngambu, A.A., Negue, E.N., Ondoa, J.M., and Nzenti, J.P., 2016, Use of Landsat 7 ETM^{+} data for the geological structure interpretation-Case study of the Ngoura-Colomines Area, Eastern Cameroon: Journal of Geosciences and Geomatics, 4(3), 61-72.